Comptes Rendus

Chimie

Gholamreza Ebrahimzadeh Rajaei, Shayan Khalili-Arjaghi, Ebrahim Fataei, Nooshin Sajjadi and Morteza Kashefi-Alasl

Fabrication and characterization of polymer-based nanocomposite membrane modified by magnetite nanoparticles for Cd^{2+} and Pb^{2+} removal from aqueous solutions

Full paper / *Mémoire*

Fabrication and characterization of polymer-based nanocomposite membrane modified by magnetite nanoparticles for Cd^{2+} and Pb^{2+} removal from aqueous solutions

Gholamreza Ebrahimzadeh Rajaei⊕ *, [a]**, Shayan Khalili-Arjaghi** [b]**, Ebrahim Fataei** [c]**,**
Nooshin Sajjadi [b] **and Morteza Kashefi-Alasl** [b]

[a] Department of Chemistry, Ardabil Branch, Islamic Azad University, Ardabil, Iran

[b] Department of Environmental Science, Marine Science and Technology, North Tehran Branch, Islamic Azad University, Tehran, Iran

[c] Department of Environmental Science, Ardabil Branch, Islamic Azad University, Ardabil, Iran

E-mails: gh.ebrahimzadeh@gmail.com (G. Ebrahimzadeh Rajaei),
shayan_yashar@yahoo.com (S. Khalili-Arjaghi), eafataei@gmail.com (E. Fataei),
nooshinsadjadi@yahoo.com (N. Sajjadi), mortezakashefialasl@gmail.com
(M. Kashefi-Alasl)

Abstract. In the present work, a polyvinyl chloride (PVC)/magnetite nanocomposite membrane (NCM) was fabricated by a casting technique for the removal of Cd^{2+} and Pb^{2+} ions from aqueous solutions. Magnetite (Fe$_3$O$_4$) nanoparticles (NPs) were synthesized from the *Ramalina sinensis* plant extract. The synthesized materials were characterized by UV–visible, X-ray diffraction, Fourier-transform infrared, field emission scanning electron microscopy, energy-dispersive X-Ray spectrometry, Brunauer–Emmett–Teller (BET) surface area analysis, vibrating sample magnetometry, and thermal gravimetric analysis techniques. The fabricated NCM enhanced the adsorption capability of PVC without the use of any catalyst. The size of the magnetite NPs distributed in the NCM structure varied in the range of 25–70 nm. The specific surface area of the fabricated NCM was found to be 5.670 m$^2 \cdot$g^{-1}, which is approximately thrice greater than the reported value for pure PVC. The removal process of both Cd^{2+} and Pb^{2+} ions from aqueous solution showed the best fit to the Langmuir isotherm model. The maximum adsorption capacities of cadmium and lead ions were estimated to be 11.55 and 11.40 mg$\cdot$g^{-1}, respectively. A kinetic investigation showed that the removal process of both metal ions can be well described by the pseudo-second-order kinetic model. The results obtained from adsorption investigations revealed that the synthesized NCM can be used for the removal of Cd^{2+} and Pb^{2+} ions from aqueous media.

* Corresponding author.

1. Introduction

Heavy metal ions severely pollute water due to their high toxicity and non-biodegradability [1]. These heavy metal ions can diffuse into the food chain of animals and eventually into human food, which can pose serious risks to human health [2]. Cadmium and lead are two very common toxic metal ions capable of inducing severe human diseases and health problems [3]. According to the World Health Organization, standards on permissible limits of cadmium and lead in water are 0.01 and 0.05 mg·L^{-1}, respectively [4]. For drinking water, standards on permissible limits of cadmium and lead are 3 and 10 µg·L^{-1}, respectively [5]. Levels above these limits can result in skin, kidney, lung, bladder, and liver cancers as well as cardiovascular and infectious diseases, tissue injury, and anemia [6,7]. Several techniques have been developed for the analytical determination of Cd^{2+} and Pb^{2+} ions among which inductively coupled plasma–optical emission spectroscopy [8], inductively coupled plasma–mass spectrometry [9], and graphite furnace atomic absorption spectrometry [10] are worth mentioning. These methods, however, require expensive equipment and trained operators. In this work, an atomic absorption spectrometer equipped with a flame atomizer was used to determine the concentration of both metal ions. This technique allows the determination of many elements with high sensitivity with efficient background correction [11].

Lichen is a composite organism produced by algae or cyanobacteria living among filaments of multiple fungi species in a mutualistic relationship [12]. Some lichens are used as medicines or food in some regions [13]. They can also serve as bio-indicators of air pollutants [14]. Recently, green nanotechnology methods have been applied to the synthesis of nanoparticles (NPs) through other simple techniques [15]. The green synthesis of NPs from natural biological resources such as lichens is an inexpensive, efficient, eco-friendly, chemical-free, and sustainable method [16]. In the past few years, some types of lichens [17], algae [18], fungi [19], and bactericidal agents [20] have been utilized to synthesize

non-toxic and useful metallic NPs. In this study, the synthesis of iron oxide NPs by the plant extract of lichen *Ramalina sinensis* (RS) was explored.

Among the different types of NPs, Fe$_3$O$_4$ NPs have exhibited various advantages in the fields of nanobiotechnology and wastewater treatment [21]. Iron oxide NPs have been gaining the attention of the research community in solving environment-related problems [22]. This is because they have a high surface-area-to-volume ratio; so their surface can be used as an excellent adsorbent to remove dyes and toxic heavy metals from aqueous solutions [23]. On the other hand, nanocomposites have been increasingly studied to be used as nanofiltration membranes for water and wastewater treatment [24–26]. Pawar *et al.* found that the adsorption capacity of iron oxide modified clay-activated carbon composite beads for the removal of hazardous lead, arsenic, and cadmium from aqueous environments was high [27]. Horst *et al.* reported high sorption capacity of magnetic nanocomposites for the removal of Cu, Zn, Cd, and Cr as heavy metals [28]. The Nayak group reported a novel modified polyvinyl chloride (PVC) blend membrane with good efficiency for the removal of heavy metal ions, namely lead, cadmium, and chromium [29]. Recently, the Farjami group fabricated a new emulsion PVC microporous nanocomposite ultrafiltration membrane [30]. The removal of heavy metals and toxic dyes from wastewater has been studied by some researchers using other new polymer-based nanocomposites [31–33]. Following the valuable studies of these researchers, this work is aimed at the fabrication of a PVC/iron oxide nanocomposite membrane (NCM) and its application in the removal of cadmium and lead ions from an aqueous solution.

Among the various polymeric materials used in the fabrication of nanofiltration membranes, PVC has exhibited higher durability and flexibility [34]. In this work, PVC and sodium dodecyl sulfate (SDS, as an anionic surfactant) were used to form a new NCM containing iron oxide NPs for the removal of Cd^{2+} and Pb^{2+} from aqueous solutions. Sodium dodecyl sulfate is also one of the most applicable surfactants in the fabrication of nanofiltration membranes

due to its high hydrophilicity and biocompatibility as well as cost-effectiveness compared with other more complex surfactants [35]. Polymer–metal NCMs are considered as a new class of adsorbents with interesting chemical and physical properties since they possess all the essential features [36]. Water treatment technologies including membrane separation [37], chemical coagulation [38] and precipitation [39], ion exchange [40], and electrochemical treatment [41] have been employed for the removal of heavy metal ions from aqueous solutions. However, among these techniques, adsorption processes are inexpensive, fast, and efficient, which enables their application to the removal of toxic metal ions [42–45].

2. Materials and methods

2.1. *Materials*

PVC (MW: 78,000 g/mol; Arvand Petrochemical Company, Iran) and SSD (MW: 288.38 g/mol; Merck, Germany) were employed as the polymer and the surfactant for the fabrication of NCM films, respectively (their structures are shown in Figure 1). Tetrahydrofuran (THF, d: 889 kg/m^3; Sigma-Aldrich, Germany) and dimethylacetamide (DMA, d: 940 kg/m^3; Sigma-Aldrich, Germany) were used as the solvents. FeCl$_2 \cdot 4H_2O$ (99%; Merck, Germany), FeCl$_3 \cdot 6H_2O$ (99%; Sigma-Aldrich, Germany), NH$_3$ (28%; Merck, Germany), and native lichen RS (collected from the Fandoqlu Forest in the southeastern region of Ardabil, Iran) were used for the synthesis of iron oxide NPs. NaOH (96%; Tianjin Yongda Chemical Reagent Company, China) and HCl (36%; Chongqing Dongchuan Chemical Company, China) were also utilized to adjust the pH of the solutions. Cadmium nitrate tetrahydrate and lead(II) nitrate (Merck, Germany) were used to prepare the required stock solution.

2.2. *Equipment*

The UV–visible spectrum of the NPs was obtained using a UV-2450 Shimadzu spectrophotometer. Fourier-transform infrared (FTIR) spectra of the PVC, iron oxide NPs, and PVC/iron oxide NCM were recorded by an FTIR Bruker spectrometer. X-ray diffraction (XRD) patterns of the synthesized iron oxide NPs and NCM were obtained by a Philips
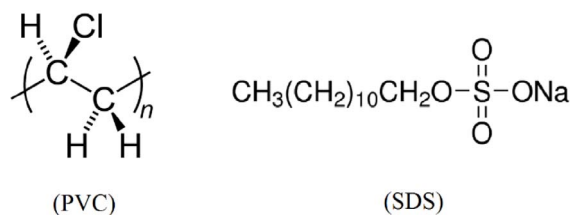

Figure 1. Structures of PVC and SDS.

PW1730 diffractometer operating with Cu Kα radiation ($\lambda = 0.154$ nm). The surface morphology of the NPs and PVC/iron oxide NCM was observed through a field emission scanning electron microscope (FE-SEM, TESCAN MIRA III). Adsorption–desorption isotherms of nitrogen were evaluated by a high-precision surface area and pore size analyzer (BEL-SORP MINI II). A vibrating sample magnetometer (VSM) with MDKF-FORC/VSM (Meghnatis-Daghigh-Kashan Co.) was also employed to study the magnetic properties of the samples. The residual concentration of Cd^{2+} and Pb^{2+} ions after the adsorption process was evaluated by a flame atomic absorption spectrophotometer (FAAS, PerkinElmer AAnalyst 300). Differential thermal gravimetric analysis (TGA/DTG) was performed by a Linseis STA PT1000 instrument.

2.3. *Synthesis of iron oxide NPs*

Iron oxide NPs were synthesized by the co-precipitation method as reported in previous work [46]. First, 10 mL of the extract obtained from the distillation of 10 g lichen RS was added to a 100 mL solution of Fe^{3+}/Fe^{2+} at a ratio of 2:1 in a 250 mL volumetric flask. The prepared solution was vigorously stirred using a magnetic stirrer at 70 °C for 1 h. During this time, 1 mL of ammonia solution (0.1 M) was added dropwise to the flask to complete the NP synthesis reaction. After decantation and filtration, the brownish NPs obtained were rapidly washed with double distilled water until the solution pH reached the neutral range near 7. The synthesized NPs were then washed with ethanol and dried in an oven at 50 °C for 24 h. They were then calcined at the range of 500–700 °C for 3 h in a muffle furnace. This black product was stored in a desiccator for later use.

2.4. *Fabrication of polymer-based NCM*

For this purpose, 85.7 mL of THF and 14.3 mL of DMA were mixed in a laboratory glass under the hood. Then, 12 g of PVC and 0.45 g of SDS were added in a conical flask; a sufficient amount of solvent mixture (85:15 wt%) was added to prepare 100 g of the mixture. The prepared mixture was vigorously stirred using a magnetic stirrer for 20 min at 25 °C, and it was then placed inside an ultrasonic device for 15 min to obtain a perfectly homogeneous mixture. To prepare NCMs containing 0.5 wt% iron oxide NPs, the same steps were followed, but 0.5 g iron oxide NPs were added in the flask before the mixture weight was increased to 100 g. Subsequently, the obtained mixtures were cast on a clean glass plate with dimensions of 20×15 cm^2 at ambient temperature by a manual casting knife with 300 µm thickness. The membrane surface was exposed to airflow at 27 °C for 30 min to evaporate the excess solvent. Then, it was immersed in a distilled water bath at ambient temperature. The polymer-based NCM layer was taken out after 20 min and then immersed again in the distilled water bath for 24 h to ensure the complete removal of the remaining solvent. The cadmium and lead removal performance of the fabricated NCMs was assessed in aqueous solutions.

2.5. *Adsorption experiments*

First, a polyvinyl syringe with a capacity of 5 mL and an effective area of 1.13 cm^2 was chosen and its plungers were removed. Then, the fabricated NCM film was cut to fit the inner diameter of the syringe (almost 12 mm) and inserted to its end. The solutions with the required concentrations of Cd(II) and Pb(II) were prepared by diluting a suitable stock solution. Different concentrations of cadmium and lead ion solutions were passed through the unused NCM film under constant pressure generated by an air cylinder, and the residual concentrations of the collected solutions were determined using an FAAS. The removal percentage (%R) of each ion was calculated by (1).

$$\%R = \frac{(C_0 - C_e)}{C_0} \times 100, \qquad (1)$$

where C_0 and C_e are the initial and equilibrium concentrations (mg·L^{-1}) of the ion solution, respectively. The removal amount of each ion, q_e (mg·g^{-1}), on the
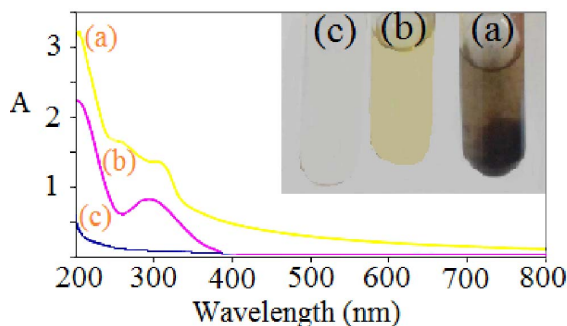

Figure 2. UV–visible absorption spectra of (a) magnetite (Fe$_3$O$_4$) NPs, (b) Fe^{3+}/Fe^{2+} (2:1 ratio) solution, and (c) RS lichen extract.

fabricated NCM film was calculated using the following equation:

$$q_e = \frac{(C_0 - C_e)}{W} \times V, \qquad (2)$$

where V (mL) and W (mg) are the volume of the solution phase and the weight of the used adsorbent, respectively. All the adsorption experiments were carried out at ambient temperature and constant pressure. A stock solution of 1000 mg·L^{-1} of each of the two ions was prepared by dissolving specific amounts of their salts in distilled water. These solutions were diluted to obtain the required solutions.

3. Results and discussion

3.1. *Characterization of iron oxide NPs and fabricated NCM*

The UV–visible absorption spectrum of the synthesized iron oxide NPs was compared with the spectrum of the Fe^{2+}/Fe^{3+} solution and the pristine RS extract shown in Figure 2. The broad absorption peak in Figure 2a corresponds to iron oxide NPs showing strong absorption at a wavelength of ~350 nm. This can be attributed to direct electron transition corresponding to the optical bandgap energy in the range of 1.92–2.87 eV [47,48]. The maximum surface plasmon resonance band of iron oxide NPs occurs at a wavelength of ~250 nm, indicating a reduction of ferric ions to iron oxide by the carbonyl of the aldehyde group existing in the RS extract [49].

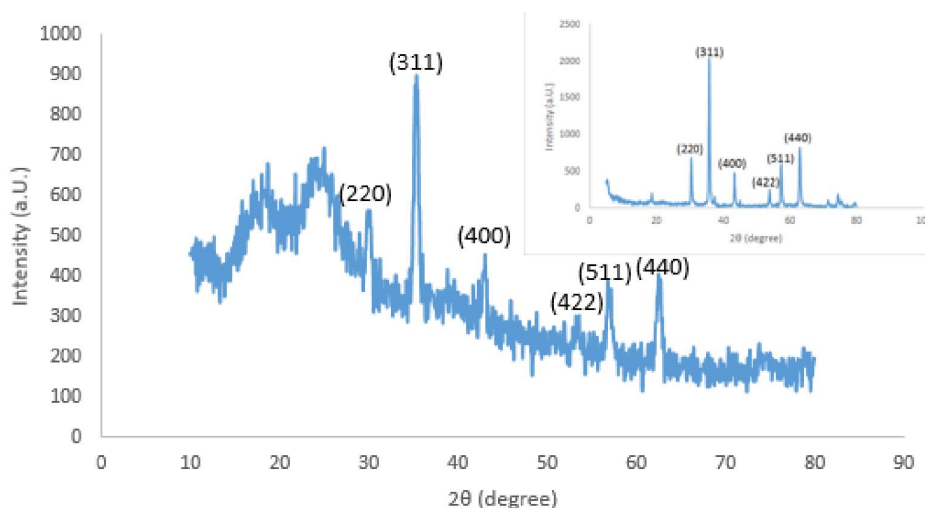The crystal structure of the products was characterized by a Philips PW1730 diffractometer. The

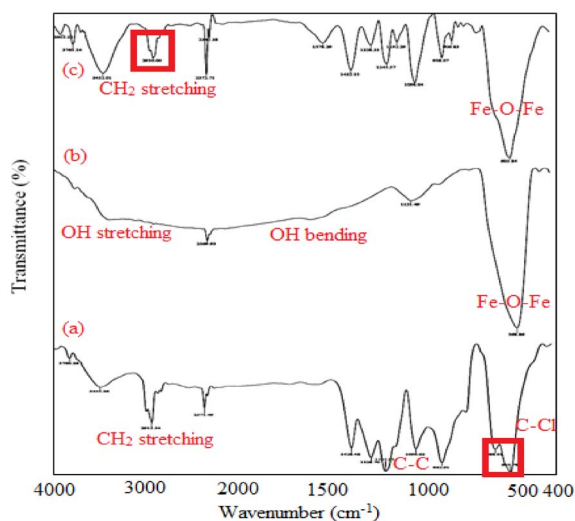**Figure 3.** XRD spectra of NCM and magnetite iron oxide NPs (inset).

Figure 4. FTIR spectra of (a) pristine PVC, (b) magnetite (Fe$_3$O$_4$) NPs, and (c) fabricated NCM.

XRD patterns of products with Cu Kα radiation (λ = 0.154 nm) were recorded in the 2θ range of 10°–80° (see Figure 3). Six characteristic peaks at 30.40° (29.88°), 35.75° (35.33°), 43.45° (42.98°), 53.80° (53.17°), 57.40° (56.92°), and 62.95° (62.61°) for iron oxide NPs (NCM) were obtained corresponding to the (220), (311), (400), (422), (511), and (440) crystal planes of pure Fe$_3$O$_4$ with a spinal structure, respectively. The XRD patterns of the prepared samples were compared with standard pattern JCPDS card no. 65-3107 [50], indicating good agreement between the obtained results and the standard values of magnetite NPs. Moreover, the diameter of NPs was evaluated ~28 nm from the (311) plane with a diffraction peak at 2θ = 35.75° using the Scherrer equation [51].

Figure 4 shows the FTIR spectrum of pristine PVC, Fe$_3$O$_4$ NPs, and fabricated NCM. According to Figure 4a, the sharp peaks at 611 and 689 cm^{-1} can be attributed to the C–Cl stretching vibrations in the PVC structure. In addition, the main peaks at 1097 and 2913 cm^{-1} are due to the C–C and C–H stretching vibrations in pure PVC, respectively. In the FTIR spectrum of Fe$_3$O$_4$ NPs (Figure 4b), the Fe–O–Fe bond stretching can be detected from the narrow peak at 569 cm^{-1}. The presence of a broad band at approximately 3500 cm^{-1} and a weak band at 1640 cm^{-1} can be attributed to the stretching and bending vibrations of the adsorbed water molecules on the iron oxide NPs, respectively [36]. The FTIR spectrum of NCM (Figure 4c) presents the characteristic absorptions of pristine PVC and Fe$_3$O$_4$ NPs but with reduced intensity of the peaks associated with oxygen–iron bonding.

The morphology of the fabricated NCM containing 0.5 wt% Fe$_3$O$_4$ NPs was examined by a field emission scanning electron microscope equipped with an energy-dispersive X-Ray spectrometer (FESEM-EDS, TESCAN MIRA III). Figures 5a–f present the surface morphology of PVC and NCM at different
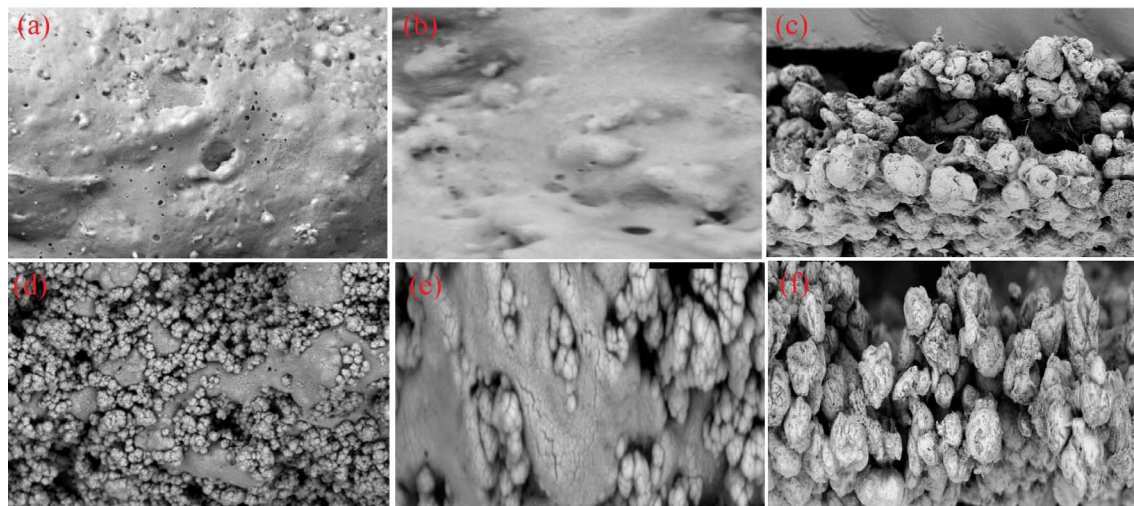
Figure 5. (a–c) FESEM images of PVC and (d–f) images of NCM containing 0.5 wt% iron oxide NPs at different magnification values of 20k, 50k, and 300k, respectively.
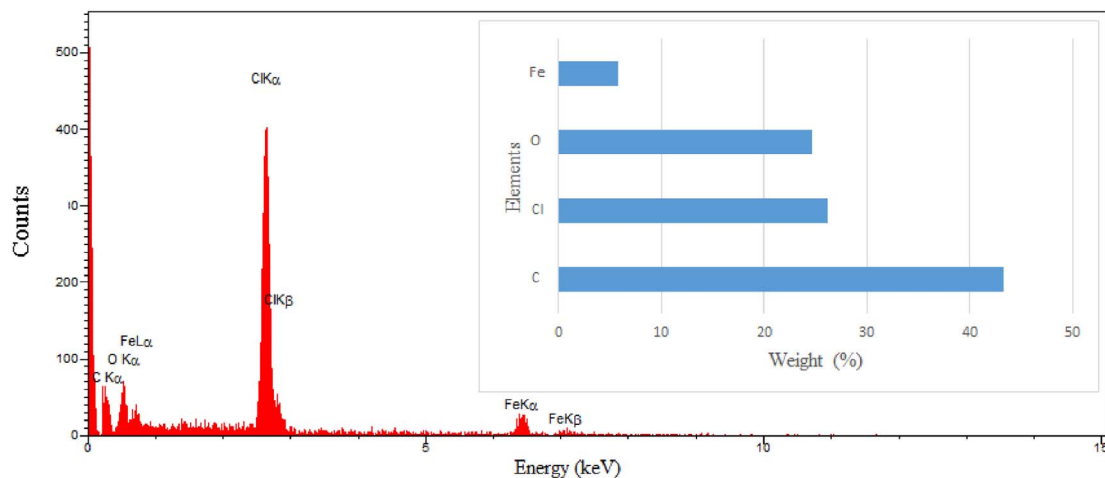

Figure 6. EDS spectrum of fabricated NCM and its elemental analysis (inset).

magnification values. The particle size of iron oxide NPs in the structure of NCM is in the range of 25–70 nm, which can be ascribed to the agglomeration of iron oxide NPs during the formation of nanocomposites as a result of Van der Waals forces and magnetic interactions between the NPs [52]. Nevertheless, the unique shape and size distribution of NPs were not observed in the SEM images. There is no unidentified peak observed in the EDS spectrum (see Figure 6), suggesting the purity of the fabricated NCM. The peaks appearing in the EDS spectrum confirmed the presence of carbon, chlorine, oxygen, and iron

elements with weight percentages of 43.25, 26.21, 24.72, and 5.82, respectively.

Figure 7 shows the adsorption–desorption isotherms of N_2 onto the NCM at a saturated vapor pressure of 84.3 kPa and a temperature of 77 K. The shape of isotherms indicates the presence of both micro- and mesopores corresponding to isotherms of Type IV. The specific surface area, pore volume, and mean pore diameter of PVC and fabricated NCM are listed in Table 1. The mean pore diameter of NCM is 7.14 nm, which belongs to the mesoporous range (2–50 nm). However, it is near the microporous
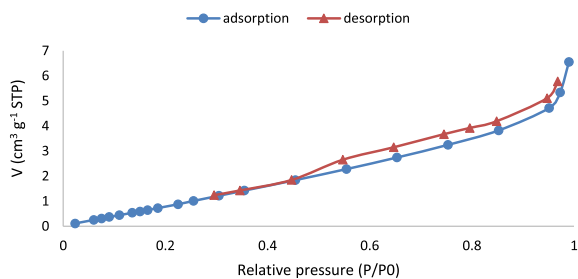
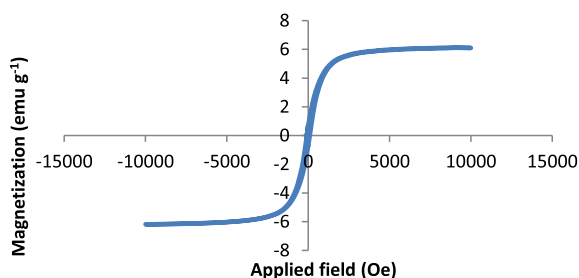**Figure 7.** N$_2$ adsorption–desorption isotherms of NCM.

Figure 8. Lack of hysteresis loop for fabricated NCM containing 0.5 wt% iron oxide NPs.

Figure 9. TGA/DTG profile of fabricated NCM containing 0.5 wt% iron oxide NPs.

range (2 nm). The fabricated NCM in this work has a specific surface area of 5.670 m$^2 \cdot$g^{-1}, which is approximately thrice greater than the reported value for pure PVC.

The magnetic properties of iron oxide NPs were measured by a VSM at a maximum applied field of 15000 Oe at ambient temperature. The magnetization plot of the fabricated NCM (Figure 8) shows no hysteresis loop and reveals a magnetic saturation of 6.11 emu·g^{-1} at room temperature. This is a significant decrease compared to the magnetic saturation of iron oxide NPs, which was reported elsewhere [54].

The TGA technique was used to determine the thermal stability of the fabricated NCM. The fraction of volatile components present in the NCM can also be determined by monitoring the weight change, which occurs as the sample is heated. The changes in the mass of PVC-based NCM as a function of temperature from 30 to 700 °C at a heating rate of 10 °C·min^{-1} were measured by TGA/DTG curves in N$_2$ atmosphere. Figure 9 shows the TGA/DTG curves of the PVC-based NCM. The slight weight loss below ~130 °C for NCM can be attributed to the evaporation of trapped THF and other volatile components.
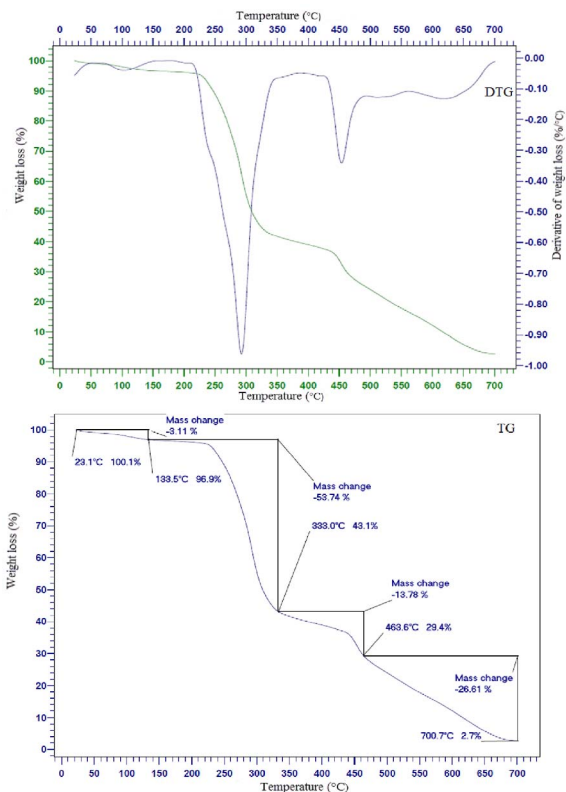
The curves in Figure 9 indicate that the fabricated NCM is remarkably stable up to 230 °C. A two-stage significant weight loss occurs in the degradation process. The first major weight loss is observed in the range of 133–333 °C, which corresponds to the loss of HCl [53]. The second major weight loss is observed in the range of 333–463 °C, which is much shorter than the first stage. Thermal degradation of the polymer backbone takes place at this stage, resulting in the formation of stable carbonaceous residue [55].

3.2. *Adsorption isotherms*

The influence of initial pH and concentration of diluted solutions on the removal percentage of Cd^{2+} and Pb^{2+} ions was investigated for various ranges at a constant dose of fabricated NCM and temperature. By considering the fact that Cd(II) and Pb(II) can generally be precipitated as hydroxides at pH values of 8.0 and 9.0, respectively, the adsorption studies were conducted in the pH range

Table 1. BET experimental data deduced from N_2 adsorption onto PVC and NCM containing 0.5 wt% iron oxide NPs

Samples	Specific surface area ($m^2 \cdot g^{-1}$)	Pore volume ($mL \cdot g^{-1}$)	Mean pore diameter (nm)	Ref.
PVC	2.018	5.467×10^{-3} (average)	26.74	[53]
NCM	5.670	10.126×10^{-3} (total)	7.14	This work

of 2.0–7.0 for Cd(II) and 2.0–8.0 for Pb(II) [56]. The pH of the solutions was adjusted by adding 0.01 M HCl or 0.01 M NaOH and measured using an electronic pH meter. The optimum conditions for the removal of ions were pH = 6 for Cd(II) and 8 for Pb(II), initial metal ion concentration = 10 mg·L^{-1}, nanocomposite dose = 150 mg/50 mL, contact time = 1 h, and temperature = 25 ± 1 °C. For the adsorption experiments, a 50 mL solution of each ion of the required concentration (5–50 mg·L^{-1}) at an optimum initial pH and nanocomposite dose was evaluated for 1 h.

The experimental data were evaluated by Langmuir and Freundlich isotherm models. The Langmuir adsorption model assumes that an adsorbent has a fixed number of binding sites. All the binding sites show the same affinity for the adsorbent. Therefore, each site adsorbs only one molecule and forms a single monolayer [57].

The linear form of the Langmuir model can be written as

$$\frac{1}{q_e} = \frac{1}{bq_m}\left(\frac{1}{C_e}\right) + \frac{1}{q_m}, \qquad (3)$$

where q_e (mg·g^{-1}) is the amount of ions adsorbed onto the NCM at equilibrium, C_e (mg·L^{-1}) is the equilibrium concentration, q_m (mg·g^{-1}) denotes the maximum adsorption capacity, and b (L·mg^{-1}) is the Langmuir constant related to free energy. The Langmuir constants q_m and b were calculated from the slope and the intercept of the Langmuir plot of $1/q_e$ versus $1/C_e$ (see Figure 10).

The linear form of the Freundlich model is given as

$$\ln q_e = \frac{1}{n}\ln C_e + \ln k_F, \qquad (4)$$

where q_e (mg·g^{-1}) represents the amount of metal ions adsorbed per unit mass of adsorbent, C_e (mg·L^{-1}) is the equilibrium concentration of metal ions, and n and k_F are Freundlich constants. These constants can be determined from the linear plot of $\ln q_e$ versus $\ln C_e$, which is shown in Figure 11. The Langmuir and Freundlich isotherm parameters for
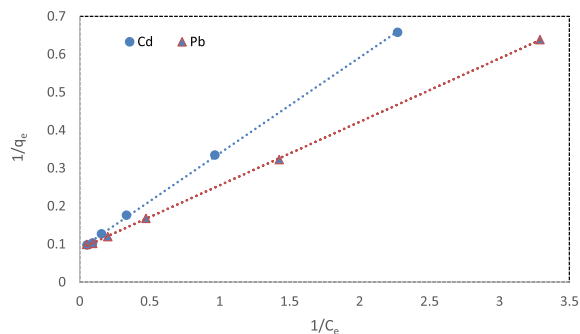
Figure 10. Linear form of Langmuir isotherm for the removal of cadmium and lead ions at 298 K.

the adsorption process of both metal ions onto the NCM are listed in Table 2. The dimensionless separation factor R_L was determined to be between 0 and 1 for both metal ion concentrations in the range of 5–50 mg·g^{-1}, indicating that the adsorption process by the fabricated NCM is favorable [58]. Moreover, n values greater than 1 from the Freundlich isotherm studies suggest favorable adsorption conditions [59]. Nevertheless, the values of the correlation coefficients showed that the removal process of both Cd^{2+} and Pb^{2+} ions from the aqueous solution can be the best fit to the Langmuir isotherm model.

3.3. *Kinetics of adsorption*

The kinetics of cadmium and lead ion adsorption onto the fabricated NCM were analyzed at various time intervals using the pseudo-first-order and pseudo-second-order kinetic models. The pseudo-first-order kinetic model is expressed as

$$\ln(q_e - q_t) = -k_1 t + \ln q_e, \qquad (5)$$

where q_t and q_e (mg·g^{-1}) are the amount of metal ions adsorbed at time t (min) and equilibrium time, respectively. The parameter k_1 (min^{-1}) denotes the rate constant of the pseudo-first-order kinetic

Table 2. Isotherm parameters and correlation coefficients (R^2) for the adsorption of cadmium and lead ions onto the fabricated NCM at 298 K

Ions	Langmuir				Freundlich		
	q_m (mg·g^{-1})	b (L·mg^{-1})	R^2	R_L	k_F	n	R^2
Cd^{2+}	11.55	0.34	0.999	0.06–0.37	2.74	1.95	0.960
Pb^{2+}	11.40	0.52	0.999	0.04–0.28	3.39	2.24	0.924
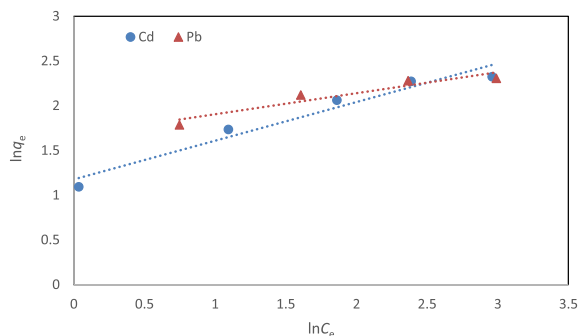
Figure 11. Linear form of Freundlich isotherm for the removal of cadmium and lead ions at 298 K.

model [60]. The rate constant of the pseudo-first-order kinetic model and $q_{e,\text{cal}}$ values are derived from the slope and the intercept of the linear plots of $\ln(q_e - q_t)$ versus time (min), respectively. The pseudo-first-order kinetic model assumes that one metal ion is sorbed onto one sorption site on the surface of an adsorbent [61].

The pseudo-second-order kinetic model can be written as

$$\frac{t}{q_t} = \frac{t}{q_e} + \frac{1}{k_2 q_e^2}, \qquad (6)$$

where k_2 (g·mg^{-1}·min^{-1}) is the rate constant of the pseudo-second-order kinetic model. This model assumes that one metal ion is sorbed onto two sorption sites on the surface of an adsorbent [62].

The rate constant of the pseudo-second-order kinetic model and $q_{e,\text{cal}}$ are estimated from the intercept and the slope of the linear plots of t/q_t versus time (min), respectively (see Figures 12a, b) [63]. Figures 12c, d indicate that with increasing initial concentration, the removal percentages of both metal ions decrease. The decrease in removal efficiency with increasing metal ion concentration may be due to the fact that with increasing metal ion concentration, more surface sites are increasingly covered,

and therefore at higher metal ion concentrations, the adsorption capacity of the nanocomposite is lost. Hence, at low concentration, the proportions of initial metal concentration to available binding sites are greater, leading to higher uptake [64,65]. As a result, lack of access to free binding sites reduces the overall removal efficiency [66]. Furthermore, it was observed that the adsorption rates of cadmium and lead on the nanocomposite were faster in the initial stages. However, the rates slowed down with the passage of time and remained almost constant after the adsorption process reached equilibrium. Overall, the trend is the same for both metal ions. That is, by increasing the contact time, there is an increase in removal percentage [22,67].

The results from kinetic studies are listed in Table 3. It is clear that the values of the regression coefficient are near unity for both metal ions ($R^2 > 0.99$) and experimental and calculated values of q_e are almost near each other. This indicates that the pseudo-second-order kinetic model fits the data well as compared to the pseudo-first-order kinetic model.

This suggests that the chemical adsorption of heavy metal ions onto the NCM is the rate-limiting step [68]. Furthermore, the importance of diffusion during the adsorption process was analyzed by the intraparticle diffusion model [69]. This model describes the movement of ions from a bulk solution to the solid phase. Plots of q_t against $t^{1/2}$ are not linear, and the lines do not pass through the origin. This means that some other processes are also involved in the adsorption. Therefore, in our case, the adsorption processes of both metal ions may not be controlled by the intraparticle diffusion kinetic model.

3.4. *Adsorption mechanism*

The adsorption mechanism depends on several factors such as binding or interaction characteristics,
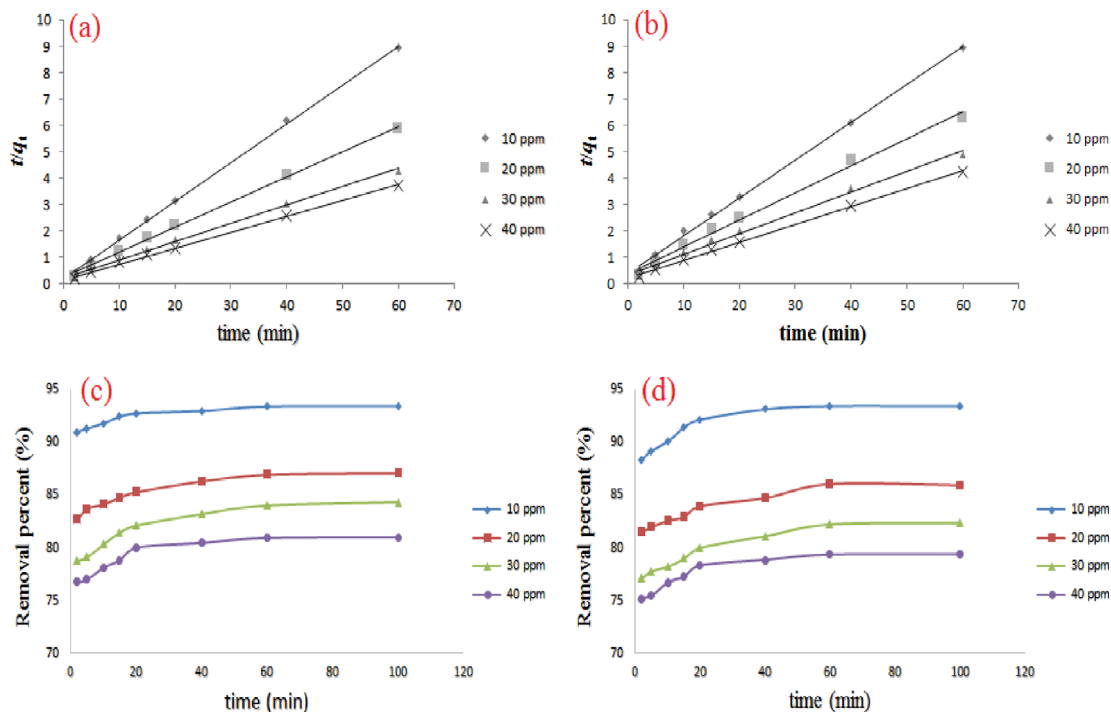
Figure 12. Pseudo-second-order kinetics for (a) cadmium and (b) lead ion adsorption onto the fabricated NCM at 298 K. Plots of removal percentage against time for (c) cadmium and (d) lead ions at various initial concentrations of 10–40 mg·L^{-1}.

Table 3. Kinetic parameters for the adsorption of cadmium and lead ions onto the fabricated NCM at 298 K

Ions	C_0 (mg·L^{-1})	$q_{e,\exp}$ (mg·g^{-1})	Pseudo-first-order kinetic model			Pseudo-second-order kinetic model		
			k_1 (min^{-1})	$q_{e,\mathrm{cal}}$ (mg·g^{-1})	R^2	k_2 (g·mg^{-1}·min^{-1})	$q_{e,\mathrm{cal}}$ (mg·g^{-1})	R^2
Cd^{2+}	10	6.73	0.047	1.22	0.904	0.127	6.78	0.999
Pb^{2+}	10	6.81	0.076	3.15	0.995	0.051	6.99	0.998

surface functional groups of adsorbents, and the chemistry of solutions [70]. The FTIR spectra of Cd(II) and Pb(II) loaded on the NCM surface were studied to determine the possible functional groups involved in the adsorption of both metal ions. In FTIR spectra, the absorption peaks of the Fe–O bond are slightly shifted to lower wavenumbers, which indicates that the Fe–O bond is involved in metal adsorption. It is evident from the results that carboxyl groups on the surface of the fabricated NCM are involved in the adsorption process. Therefore, overall, the adsorption mechanism includes both electronic attraction and chemical adsorption.

4. Conclusions

Spinal magnetite NPs were successfully synthesized using the RS extract, which were then used to prepare a polymer-based NCM using a casting technique. The samples were successfully characterized by UV–visible, X-ray diffraction, Fourier-transform infrared, field emission scanning electron microscopy, energy-dispersive X-Ray spectrometry, BET, and vibrating sample magnetometry techniques. The fabricated NCM was applied to the removal of cadmium and lead metal ions from aqueous solutions. The present study showed that the fabricated NCM can remove

toxic heavy metal ions from aqueous solutions with a high percentage of up to ~95% at low concentrations. The adsorption process reached equilibrium within 60 min at room temperature. The maximum removal of Cd^{2+} and Pb^{2+} ions from aqueous solutions was achieved at pH values of 6 and 8, respectively. The isotherm studies of both cadmium and lead ions revealed that the adsorption process followed well the Langmuir isotherm model. The kinetics of adsorption of both metal ions were found to be the best fit to the pseudo-second-order kinetic model. The adsorption mechanism included both electronic attraction and chemical adsorption.

Conflicts of interest

The authors declare no competing financial interests or personal relationships that could have influenced the work reported in this paper.

Acknowledgments

References

[1] J. Barton, M. B. G. García, D. H. Santos, P. Fanjul-Bolado, A. Ribotti, M. McCaul, D. Diamond, P. Magni, *Microchim. Acta*, 2016, **183**, 503-517.

[2] B. Nagy, A. Maicaneanu, C. Indolean, S. Burca, L. Silaghi-Dumitrescu, C. Majdik, *Acta Chim. Sloven.*, 2013, **60**, 263-273.

[3] C. Tan, Y. Moo, M. M. Jafri, H. Lim, *Optical Sensing and Detection III*, International Society for Optics and Photonics, 2014.

[4] P. Wongsasuluk, S. Chotpantarat, W. Siriwong, M. Robson, *Environ. Geochem. Health*, 2014, **36**, 169-182.

[5] F. Edition, *WHO Chron.*, 2011, **38**, 104-108.

[6] J. Huff, R. M. Lunn, M. P. Waalkes, L. Tomatis, P. F. Infante, *Int. J. Occupat. Environ. Health*, 2007, **13**, 202-212.

[7] P. J. Landrigan, C. B. Schechter, J. M. Lipton, M. C. Fahs, J. Schwartz, *Environ. Health Perspect.*, 2002, **110**, 721-728.

[8] E. dos Santos Silva, L. O. Correia, L. O. dos Santos, E. V. dos Santos Vieira, V. A. Lemos, *Microchim. Acta*, 2012, **178**, 269-275.

[9] A. A. Ammann, *J. Mass Spectrom.*, 2007, **42**, 419-427.

[10] Z. Ajtony, N. Szoboszlai, E. K. Suskó, P. Mezei, K. György, L. Bencs, *Talanta*, 2008, **76**, 627-634.

[11] S. L. Ferreira, M. A. Bezerra, A. S. Santos, W. N. dos Santos, C. G. Novaes, O. M. de Oliveira, M. L. Oliveira, R. L. Garcia, *TrAC Trends Anal. Chem.*, 2018, **100**, 1-6.

[12] R. Rosentreter, D. J. Eldridge, M. Westberg, L. Williams, M. Grube, *Biological Soil Crusts: An Organizing Principle in Drylands*, Springer, Cham, Switzerland, 2016, doi:10.1007/978-3-319-30214-0_7.

[13] W.-C. Li, J. Zhou, S.-Y. Guo, L.-D. Guo, *Fung. Div.*, 2007, **25**, 69-80.

[14] R. Sett, M. Kundu, *Donnish J. Res. Environ. Stud.*, 2016, **3**, 17-24.

[15] M. Reveathy, A. Mathiazhagan, G. Annadurai, *Eur. J. Biomed. Pharmaceu. Sci.*, 2015, **2**, 348-361.

[16] M. Iqbal, J. Bakht, *Pak. J. Bot.*, 2019, **51**, 1853-1857.

[17] Z. Çıplak, C. Gökalp, B. Getiren, A. Yıldız, N. Yıldız, *Green Process. Synth.*, 2018, **7**, 433-440.

[18] H. El-Rafie, M. El-Rafie, M. Zahran, *Carbohydr. Polym.*, 2013, **96**, 403-410.

[19] Z. Molnár, V. Bódai, G. Szakacs, B. Erdélyi, Z. Fogarassy, G. Sáfrán, T. Varga, Z. Kónya, E. Tóth-Szeles, R. Szűcs, *Sci. Rep.*, 2018, **8**, 1-12.

[20] H. Moradpoor, M. Safaei, F. Rezaei, A. Golshah, L. Jamshidy, R. Hatam, R. S. Abdullah, *Open Access Macedon. J. Med. Sci.*, 2019, **7**, 2757.

[21] L. Zhang, F. Gu, J. Chan, A. Wang, R. Langer, O. Farokhzad, *Clin. Pharmacol. Therapeut.*, 2008, **83**, 761-769.

[22] M. Jain, M. Yadav, T. Kohout, M. Lahtinen, V. K. Garg, M. Sillanpää, *Water Resour. Ind.*, 2018, **20**, 54-74.

[23] N. Neyaz, W. A. Siddiqui, K. K. Nair, *Int. J. Environ. Sci.*, 2014, **4**, 472-483.

[24] A. Gholami, A. Moghadassi, S. Hosseini, S. Shabani, F. Gholami, *J. Ind. Eng. Chem.*, 2014, **20**, 1517-1522.

[25] T.-Y. Liu, Z.-H. Liu, R.-X. Zhang, Y. Wang, B. Van der Bruggen, X.-L. Wang, *J. Membr. Sci.*, 2015, **488**, 92-102.

[26] V. Vatanpour, S. S. Madaeni, S. Moradian, S. Zinadini, B. Astinchap, *J. Membr. Sci.*, 2011, **375**, 284-294.

[27] R. R. Pawar, M. Kim, J.-G. Kim, S.-M. Hong, S. Y. Sawant, S. M. Lee, *Appl. Clay Sci.*, 2018, **162**, 339-350.

[28] M. F. Horst, M. Alvarez, V. L. Lassalle, *Separat. Sci. Technol.*, 2016, **51**, 550-563.

[29] V. Nayak, M. Jyothi, R. G. Balakrishna, K. Padaki, S. Deon, *J. Hazard. Mater.*, 2017, **331**, 289-299.

[30] M. Farjami, V. Vatanpour, A. Moghadassi, *Chem. Eng. Res. Des.*, 2020, **153**, 8-20.

[31] R. Das, V. S. Sypu, H. K. Paumo, M. Bhaumik, V. Maharaj, A. Maity, *Appl. Catal. B: Environ.*, 2019, **244**, 546-558.

[32] G. Sharma, D. Pathania, M. Naushad, *Ionics*, 2015, **21**, 1045-1055.

[33] E. N. Zare, A. Motahari, M. Sillanpää, *Environ. Res.*, 2018, **162**, 173-195.

[34] E. Radzyminska-Lenarcik, K. Witt, *Polymers*, 2019, **11**, 513.

[35] A. Mizerski, S. Neffe, *Biulet. Wojsk. Akadem. Techn.*, 2012, **61**, 395-412.

[36] S. Mallakpour, A. Abdolmaleki, H. Tabebordbar, *Eur. Polym. J.*, 2016, **78**, 141-152.

[37] M. Chen, N. P. Hankins, *J. Water Process Eng.*, 2020, **34**, article ID 101170.

[38] P. D. Johnson, P. Girinathannair, K. N. Ohlinger, S. Ritchie, L. Teuber, J. Kirby, *Water Environ. Res.*, 2008, **80**, 472-479.

[39] B. A. AbiD, M. M. BrbootI, N. M. Al-ShuwaikI, *Eng. Technol. J.*, 2011, **29**, 595-612.

[40] Z. Hubicki, D. Kołodyńska, *Ion Exchange Technol.*, 2012, 193-240.

[41] T.-K. Tran, K.-F. Chiu, C.-Y. Lin, H.-J. Leu, *Int. J. Hydrog. Energy*, 2017, **42**, 27741-27748.

[42] K. Kadirvelu, K. Thamaraiselvi, C. Namasivayam, *Bioresour. Technol.*, 2001, **76**, 63-65.

[43] A. M. Showkat, Y.-p. Zhang, M. S. Kim, A. I. Gopalan, K. R. Reddy, K. Lee, *Bullet.-Kor. Chem. Soc.*, 2007, **28**, 1985.

[44] M. A. Tofighy, T. Mohammadi, *J. Hazard. Mater.*, 2011, **185**, 140-147.

[45] Y. Xiao, H. Liang, W. Chen, Z. Wang, *Appl. Surface Sci.*, 2013, **285**, 498-504.

[46] R. Safarkar, G. Ebrahimzadeh Rajaei, S. Khalili-Arjagi, *Asian J. Nanosci. Mater.*, 2020, **3**, 157-166.

[47] S. Saha, M. Jana, P. Khanra, P. Samanta, H. Koo, N. C. Murmu, T. Kuila, *RSC Adv.*, 2016, **6**, 1380-1387.

[48] A. Mirzaei, K. Janghorban, B. Hashemi, S. R. Hosseini, M. Bonyani, S. G. Leonardi, A. Bonavita, G. Neri, *Process. Appl. Ceram.*, 2016, **10**, 209-217.

[49] N. Latha, M. Gowri, *Synthesis*, 2014, **3**, 1551-1556.

[50] P. Loekitowati Hariani, M. Faizal, R. Ridwan, M. Marsi, D. Setiabudidaya, *Int. J. Environ. Sci. Dev.*, 2013, **4**, 336-340.

[51] U. Holzwarth, N. Gibson, *Nat. Nanotechnol.*, 2011, **6**, 534-534.

[52] K. Raja, M. M. Jaculine, M. Jose, S. Verma, A. Prince, K. Ilangovan, K. Sethusankar, S. J. Das, *Superlatt. Microstruct.*, 2015, **86**, 306-312.

[53] M. Hasan, A. N. Banerjee, M. Lee, *J. Indust. Eng. Chem.*, 2015, **21**, 828-834.

[54] A. Bezaatpour, F. Payami, H. Eskandari, *C. R. Chim.*, 2017, **20**, 910-920.

[55] M. Kawasumi, N. Hasegawa, M. Kato, A. Usuki, A. Okada, *Macromolecules*, 1997, **30**, 6333-6338.

[56] M. Jain, V. K. Garg, K. Kadirvelu, *Desalin. Water Treat.*, 2014, **52**, 5681-5695.

[57] R. Saadi, Z. Saadi, R. Fazaeli, N. E. Fard, *Korean J. Chem. Eng.*, 2015, **32**, 787-799.

[58] G. E. Rajaei, H. Aghaie, K. Zare, M. Aghaie, *Res. Chem. Intermed.*, 2013, **39**, 3579-3594.

[59] A. H. Mahvi, M. Mohammadi, M. Vosoughi, A. Zahedi, B. Hashemzadeh, A. Asadi, S. Pourfadakar, *Health Scope*, 2016, **5**, 11-18.

[60] A. A. Abdelhafez, J. Li, *J. Taiwan Inst. Chem. Eng.*, 2016, **61**, 367-375.

[61] H. Yuh-Shan, *Scientometrics*, 2004, **59**, 171-177.

[62] Y. Liu, *Colloids Surfaces A: Physicochem. Eng. Asp.*, 2008, **320**, 275-278.

[63] E. D. Asuquo, A. D. Martin, *J. Environ. Chem. Eng.*, 2016, **4**, 4207-4228.

[64] M. Jain, V. Garg, K. Kadirvelu, *Bioresour. Technol.*, 2013, **129**, 242-248.

[65] M. Jain, V. K. Garg, R. Paliwal, K. Kadirvelu, S. Chaudhry, *Toxin Rev.*, 2020, 1-10, doi:10.1080/15569543.2020.1718163.

[66] H. Guo, S. Zhang, Z. Kou, S. Zhai, W. Ma, Y. Yang, *Carbohydr. Polym.*, 2015, **115**, 177-185.

[67] Z. Rafiq, R. Nazir, M. R. Shah, S. Ali, *J. Environ. Chem. Eng.*, 2014, **2**, 642-651.

[68] S. Liang, X. Guo, N. Feng, Q. Tian, *J. Hazard. Mater.*, 2010, **174**, 756-762.

[69] S. W. Hong, S. H. Ahn, O. K. Kwon, J. D. Chung, *J. Mech. Sci. Technol.*, 2014, **28**, 1985-1993.

[70] N. Kataria, V. Garg, *Chemosphere*, 2018, **208**, 818-828.